

DIRECT NUMERICAL SIMULATIONS OF TURBULENCE INDUCED SECONDARY MOTION IN SQUARE AND SKEWED DUCTS

Hassan Raiesi, Andrew Pollard and Ugo Piomelli

Department of Mechanical and Materials Engineering
Queen's University, Kingston (ON) K7L 3N6, Canada

ABSTRACT

We performed direct numerical simulations of turbulent flow in square and skewed ducts. A second-order-accurate finite-volume approach was used to discretize the Navier-Stokes equations in a curvilinear coordinate system. The mean secondary flow field was observed in all cases; in the skewed ducts, however, the strength of the secondary flow is weaker compared to that for the square duct. The flow in the sharper corners tend to relaminarize and the axis of the secondary flow shifts toward the corner with wider angle.

1 Introduction

The study of turbulent flows in corners of two solid boundaries is of great importance, as they are encountered in many flow devices, such as the wing-body junction of an aircraft, winglets and tube bundles in heat exchangers. Due to the significant anisotropy, complex flow structures are formed in these areas, which cannot be captured by isotropic eddy-viscosity-based turbulence models (Speziale, 1987; Wallin & Johansson, 2000).

Early measurements of the flow in square ducts performed by Nikuradse (see Schlichting (1979), p. 612) revealed the existence of the mean secondary flow in the plane normal to the mean streamwise velocity. This type of secondary flow is known as “stress-induced secondary flows” (Bradshaw, 1987) and is due to the anisotropy of the normal Reynolds stresses. The effect of the secondary flow is to transport slow-moving fluid away from the wall at the duct centre, while moving fast-moving fluid from the duct core towards the corner, increasing the wall stress there. Further experiments were conducted by Brundrett & Baines (1964); Gessner & Jones (1965); Gessner (1973), while direct numerical simulations (DNS) were performed by Gavrilakis (1992); Huser & Biringen (1993); Uhlmann *et al.* (2007); Pinelli *et al.* (2010). All these works confirm the presence of two counter-rotating vortices symmetrically placed about the diagonals of the cross-section,

and also showed that the turbulent statistics are in very good agreement with the plane channel data along the wall bisector. Pinelli and co-workers (Uhlmann *et al.*, 2007; Pinelli *et al.*, 2010) studied the Reynolds number dependence of mean flow structures in a square duct for a range of Reynolds numbers. They showed that the distribution of mean streamwise vorticity is not due to the presence of two large vortices, but rather by a higher probability of the existence of vorticity of a given sign in the buffer layer. They also showed that the center of the mean secondary flow remains at a constant location for large Reynolds numbers.

In this paper we aim to extend the studies mentioned above by performing DNS of the flow in skewed ducts, to determine how shallower or sharper angles affect the flow dynamics. The Reynolds number based on the bulk velocity and half square root of the area of the cross section of the duct, Re_b , is approximately 2,200, similar to that of other DNS studies by Gavrilakis (1992); Pinelli *et al.* (2010). A square duct and two skewed ones, with angles of 30 and 60 degrees, were simulated. In the following we first present the governing equations and boundary conditions, and describe the numerical algorithm. We then discuss the numerical results, and finish with conclusions and recommendations for future work.

2 Problem formulation

The governing equations are the equations of conservation of mass and momentum for an incompressible fluid. In dimensionless form they are:

$$\frac{\partial u_i}{\partial x_i} = 0; \quad \frac{\partial u_i}{\partial t} + \frac{\partial u_j u_i}{\partial x_j} = -\frac{\partial p}{\partial x_i} + \frac{1}{Re} \nabla^2 u_i - \delta_{ij} f \quad (1)$$

In the above equations Re is the Reynolds number based on the average shear velocity, $u_\tau = (\tau_w/\rho)^{1/2}$ and L_r , the square root of the cross-sectional area, p is the pressure divided by density, x_i are the Cartesian coordinates

and u_i are the components of the velocity vector.

The Navier-Stokes equations were discretized using a finite-volume method on a co-located grid arrangement in curvilinear coordinates. A second-order scheme was used to approximate both the viscous and non-linear terms, and a fractional step algorithm was used to integrate the equations in time using a fully explicit second-order Adams-Bashforth method (Mahesh *et al.*, 2004; Kim & Moin, 1985). The discretization of the Poisson equation in general coordinates results in a system of linear equations with 19 non-zero diagonal terms, solved using an algebraic multi-grid technique, which treats all the off-diagonal terms implicitly to overcome any stability and accuracy issues. This method ensures that the velocity field is divergence free up to the machine zero after each time step.

Periodic boundary conditions are used in the streamwise direction, and no-slip boundary conditions are applied at the solid boundaries. It is also assumed that the flow is fully developed in the duct, and a constant mean pressure gradient f is applied to drive the flow in the periodic streamwise direction: $\tau_w P/A = f$, where P and A are the perimeter and the cross sectional area of the duct respectively and τ_w is the mean wall shear stress.

The dimension of the computational domain for the flow in a square duct is $12 \times 2 \times 2$ in streamwise and cross stream directions respectively. For the skewed duct, the cross stream length of the domain was scaled to fix the Reynolds number based on the average shear velocity to 150 for all cases. The length of the sides of the duct is given by $L = 2h = 2/(\sin \alpha)^{1/2}$, which fixes the cross sectional area of the duct and the average wall shear stress. Therefore, the Reynolds number defined based on this scales will be constant for the flow in square and skewed ducts if the constant pressure gradient used to drive the flow is also scaled by P/A .

For the square duct, simulations were carried out on two grids: a coarse one that used $241 \times 121 \times 121$ grid points, and a finer with $361 \times 181 \times 181$ points. The resolution of the first simulation was $\Delta x^+ = 7.5$, $\Delta y^+, \Delta z^+ < 4.2$, while for the second $\Delta x^+ = 5$, $\Delta y^+, \Delta z^+ < 2.0$. For the skewed-duct cases we used $361 \times 241 \times 241$ grid points in streamwise and cross-stream directions respectively, to discretize a domain of length 12 and sides L (defined above). An example of the grid for the $\alpha = 30^\circ$ case is shown in Figure 1.

In all simulations, the time step size was limited to ensure $CFL < 0.3$. It should be noted that for DNS of turbulent flows the viscous stability limit of time-step size is less restrictive than the accuracy and convective time-step limitation for $Re \gg 1$; therefore, a fully explicit scheme can be used. In all cases the governing equations were integrated for a dimensionless time $tu_\tau/L_r = 55$ after a statistically stationary state had been reached. The statistics were also averaged over quad-

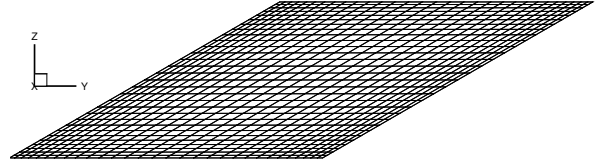


Figure 1. Grid for the $\alpha = 30^\circ$ case.

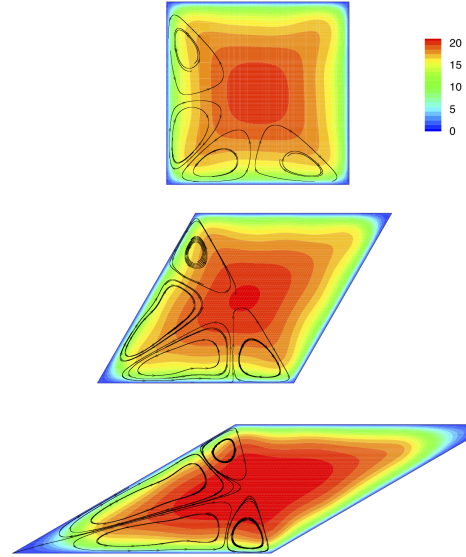


Figure 2. Mean streamwise velocity contours and streamlines of the mean secondary flow.

rants to increase the sample size. In the following, mean quantities will be denoted by angle brackets $\langle \cdot \rangle$, while a prime will denote the turbulent fluctuations.

3 Results

In order to validate the computational code, the results of the $Re_b = 2236$ simulation of the square duct were examined. First, we verified that grid convergence had been achieved by comparing the results on the coarse and fine meshes, which were found to differ by less than 3%. Secondly, we compared the results with those obtained by Pinelli *et al.* (2010), who performed DNS of the square duct at various Reynolds numbers using a pseudo-spectral method. Excellent agreement was obtained for first- and second-order moments.

The mean streamwise velocity and streamlines of the secondary flow are presented in Figure 2. The pattern of the secondary flow is similar in all cases: two counter rotating vortices are observed at each corner,

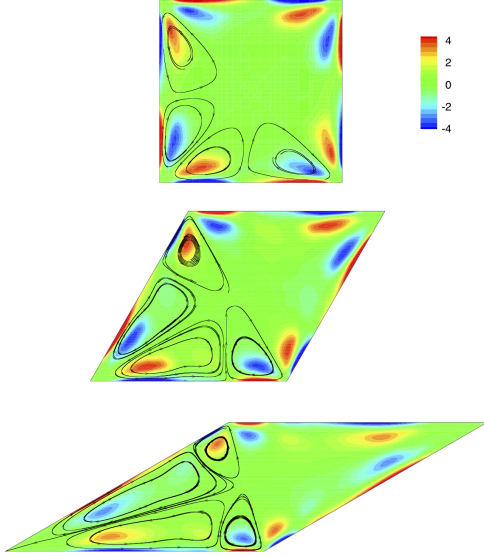


Figure 3. Mean streamwise vorticity contours and streamlines of the mean secondary flow.

with the secondary flow directed towards the corners. For the skewed ducts, the pattern is highly asymmetric; the vortex closer to the acute angle being more elongated than the other. Also, the vortex center moves away from the acute corner. This is due to a quasi-laminarization of the flow in the smaller corner that will be discussed later. Although the secondary vortices are quite asymmetric, the maximum vorticity is nearly equal, as shown in Figure 3. The shear generated at the wall to satisfy the no-slip condition is almost twice as large as the vorticity due to the rotational motion.

Figure 4 shows the distribution of the streamwise and lateral components of the wall stress,

$$\tau_{w,x} = \frac{1}{Re} \frac{\partial U}{\partial z} \quad \text{and} \quad \tau_{w,z} = \frac{1}{Re} \frac{\partial V}{\partial z}. \quad (2)$$

Note that the lateral stress is 10% of the streamwise one, while the maximum cross-stream velocity is only 5% of the mean streamwise one. This is another indication that the secondary flow, although weak, has a significant effect on the momentum transfer. Also notice how in the skewed ducts the region of strong lateral stress almost disappears near the acute angle, and the only region where a significant lateral stress occurs is near the obtuse angle.

Figure 5 shows instantaneous flow visualizations for the three cases. The most notable difference between the three cases is the quiescent nature of the flow in the acute corner, which is highlighted by the ab-

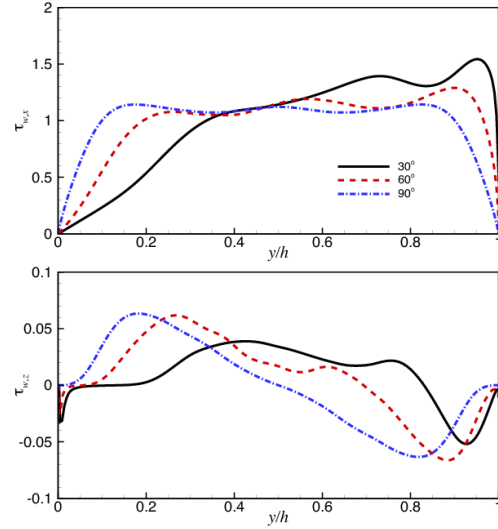


Figure 4. Profile of the wall stress. (a) Streamwise component; (b) spanwise component.

sence of vortical structures and by the disappearance of the near-wall streaks (Figure 5(a)). Furthermore, while near the obtuse corner the wall stress is predominantly larger than the mean (whose value is unity because of the normalization used), near the acute corner it is negligible. A similar phenomenon had been observed in the flow over riblets by Choi *et al.* (1993). However, in their case the distance between the riblet tips was either 40 or 20 wall units, and the quasi-streamwise vortices, whose average size is $d^+ \simeq 30$, could not penetrate the space between the riblets. In our case we observe no quasi-streamwise vortices in regions where the distance between the walls is much larger, of the order of 50 wall units. It is as yet unclear why the vortices do not penetrate further into the acute angle.

Pinelli *et al.* (2010) have recently shown that secondary flow in a square duct is governed by the buffer layer structures and is due to the preferred positioning of the high speed streaks in the near-wall region. They presented the probability density function of streak locations and its correlation with the wall shear distribution as the supporting evidence. In a square duct, there is a high probability of hosting a high speed-streak near the corner regions where a peak in the wall shear distribution is observed. We repeated the same study here using the data obtained for the skewed ducts. The results are plotted in figure 6. It shows that there is a much higher probability of high-speed streak near the obtuse angle, while in the regions near the acute angle the flow is more quiescent.

The contours of Reynolds stresses for the $\alpha = 30^\circ$ case are shown in Figure 7. The stress tensor is rotated to a coordinate system aligned with the diagonals of the duct. The streamwise normal stress, $\langle u'_1 u'_1 \rangle$ is nearly

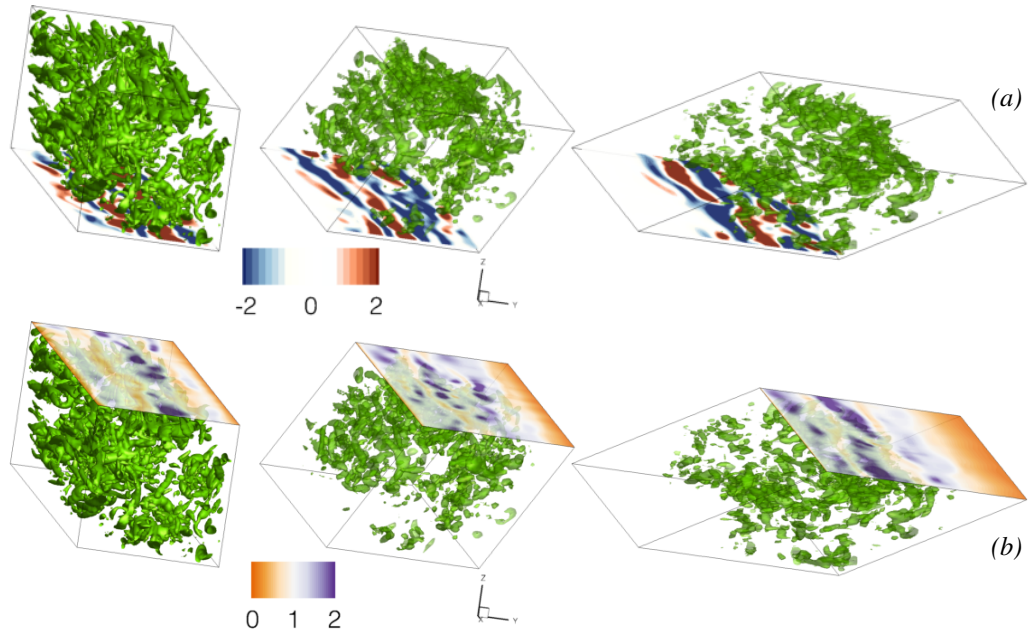


Figure 5. Isosurfaces of Q and (a) contours of u' on a plane at $y^+ = 7.5$, (b) contours of the streamwise component of the wall stress.

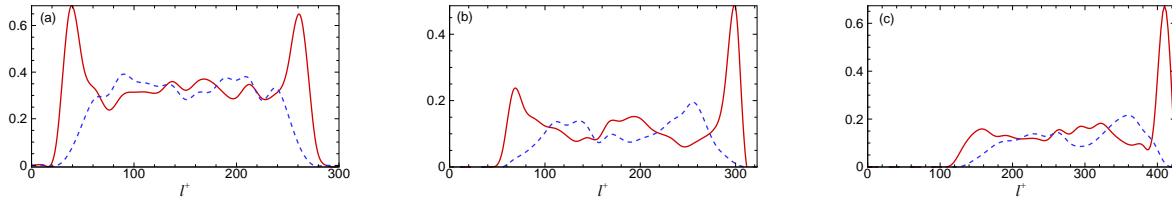


Figure 6. Probability density function of streak locations along the duct side; (a) square duct, (b) D60 duct, (c) D30 duct; — high-speed streaks; --- low-speed streaks.

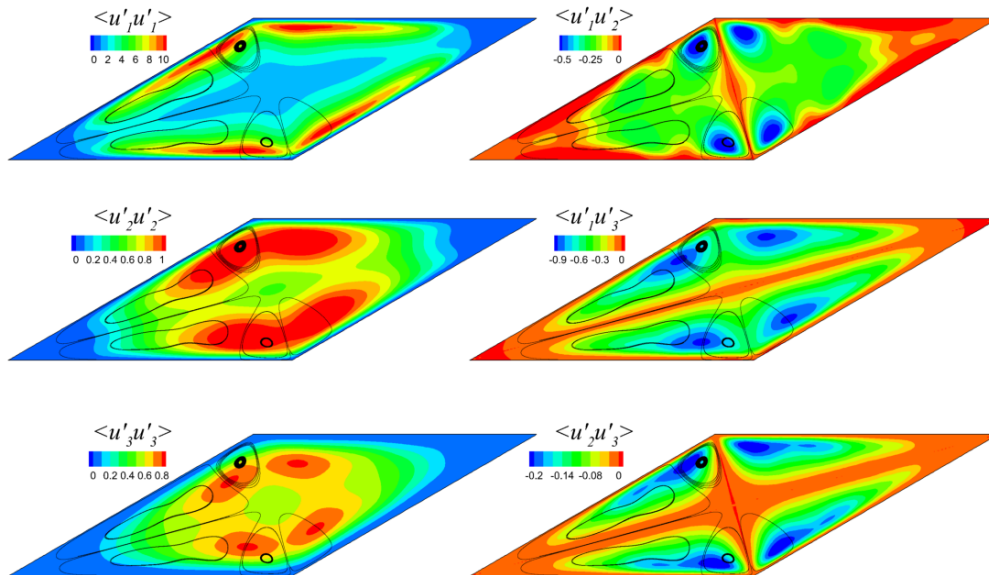


Figure 7. Mean Reynolds-stress contours for the $\alpha = 30^\circ$ case.

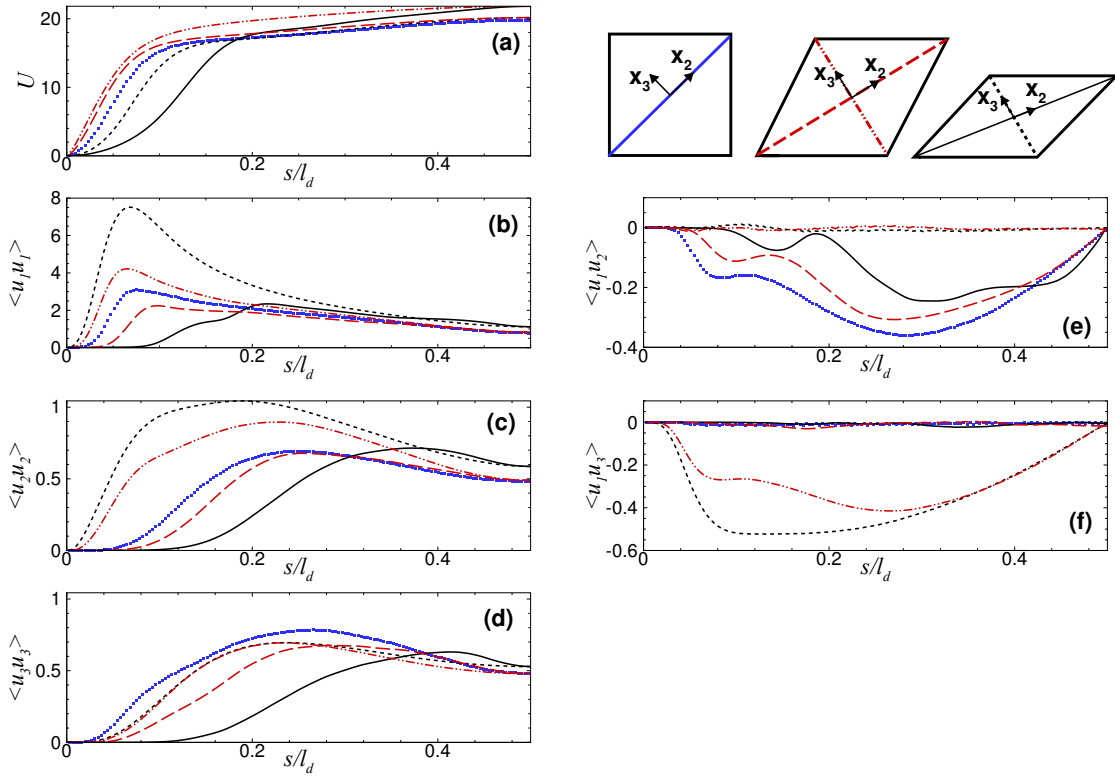


Figure 8. Profiles of mean velocity and Reynolds stresses along the duct diagonals. ■ $\alpha = 90^\circ$; --- $\alpha = 60^\circ$, long diagonal; - - - $\alpha = 60^\circ$, short diagonal; — $\alpha = 30^\circ$, long diagonal; ····· $\alpha = 30^\circ$, short diagonal.

uniform in the direction parallel to the walls, and depends mainly on distance from the nearest wall. The other two normal stresses, $\langle u_2 u_2 \rangle$ and $\langle u_3 u_3 \rangle$, tend to concentrate in the obtuse corner region. The main shear components, $\langle u_1 u_2 \rangle$ and $\langle u_1 u_3 \rangle$, peak in the upwash region between the vortices. This is also the region where the wall stress is maximum.

We observe a significant decrease of the cross-stream normal stresses in the sharp corner, and also a decrease of the shear stresses, which are responsible for the production of turbulent kinetic energy. In this region, the predominance of viscous dissipation over the production seems to be responsible for the relaminarization. An analysis of the Reynolds-stress budgets, however, is required to identify whether turbulent diffusion and pressure also play a part. The strong anisotropy of the Reynolds stresses is also evidenced.

Figure 8 shows the profiles of mean velocity and Reynolds stresses along the two diagonals of the ducts. Here, l_d is the length of the diagonal. The tendency to relaminarization in the acute corners can be seen very clearly: the velocity profile changes concavity near the corner, where the fluid slows down considerably due to the increased viscous stress. While the streamwise stress does not change appreciably, the two cross-stream components decrease significantly in the sharp corner. The shear components of the Reynolds stress tensor

are also significantly decreased in the corner, especially $\langle u_1 u_2 \rangle$ and $\langle u_2 u_3 \rangle$ ($\langle u_2 u_3 \rangle$ does not contribute to the transport of streamwise momentum). The lack of cross-stream turbulent transport indicates that in this area turbulence may become “inactive”, as the shear stresses decrease more rapidly than the turbulent kinetic energy itself. The residual turbulent motions are then mostly advected, and no production takes place. Note also that the secondary shear stress $\langle u_2 u_3 \rangle$ has a magnitude comparable to that of the primary one, $\langle u_1 u_2 \rangle$, despite the fact that the maximum velocity of the secondary flow is much smaller than the streamwise velocity.

Figure 9 presents the scaling of the streamwise velocity component at the wall bisector. For all cases there exists a logarithmic region where the velocity scales with the average shear velocity, u_τ , i.e. $U^+ = 3.2 \log(z^+) + 4$ for the square duct. However, the constants of the logarithmic fit are different from their values for turbulent flows near solid boundaries where there is no secondary motion (i.e plain turbulent channel flow). The deviation from the square duct for the case of the 30 degree duct, indicates a stronger influence of the secondary motion on mean streamwise velocity.

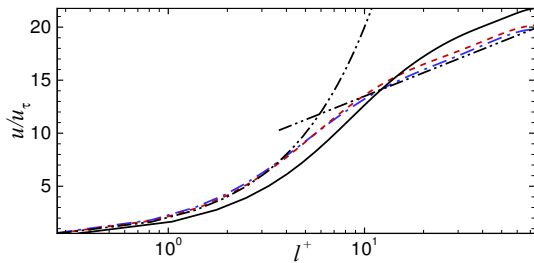


Figure 9. Profile of the mean streamwise velocity at the wall bisector, — · — $\alpha = 90^\circ$; - - - $\alpha = 60^\circ$; — $\alpha = 30^\circ$; - · - logarithmic fit.

4 Conclusion

Direct numerical simulation of fully developed turbulent flows through ducts at a bulk Reynolds number of 2236 have been performed. The mean secondary flow was observed all cases; the maximum magnitude of the velocity of the mean secondary flow in the cross-stream plane is about 5% of the mean streamwise velocity. The secondary flow, however, results in increases of up to 50% in the wall stress, strong anisotropy of the Reynolds stresses, and secondary shear stresses, that are as large as the primary ones.

The secondary flow highly skews the distribution of the wall shear stress. A secondary wall stress, in the cross-stream direction, is also generated. The flow in the corner tends to relaminarize in the sharper corner for the two skewed ducts; this phenomenon is especially strong in the $\alpha = 30^\circ$ case. While the streamwise stresses $\langle u'u' \rangle$ are not very significantly altered, the fluctuations in the cross-plane are much reduced. This results in a reduction of the shear stresses, and, hence, decreased production; the “inactive” turbulence is advected only, and does not participate actively to the turbulence generation.

Further studies of the vorticity and Reynolds stress budgets are ongoing to elucidate better the transport mechanisms. Also, simulations at higher Reynolds number are planned, to limit transitional effects.

Acknowledgments

The authors thank the High Performance Computing Virtual Laboratory (HPCVL), Queen’s University site, for the computational support. This research was partly supported by NSERC and Bombardier Aerospace. UP acknowledges the support of the Canada Research Chairs Programme; AP the support of the Queen’s Research Chairs Programme.

REFERENCES

Bradshaw, P. 1987 Turbulent secondary flows. *Annu. Rev. Fluid Mech.* **19** (1), 53–74.

- Brundrett, E. & Baines, W. D. 1964 The production and diffusion of vorticity in a square duct. *J. Fluid Mech.* **19**, 375–394.
- Choi, H., Moin, P. & Kim, J. 1993 Direct numerical simulation of turbulent flow over riblets. *J. Fluid Mech.* **255**, 503–539.
- Gavrilakis, S. 1992 Numerical simulation of low-Reynolds-number turbulent flow through a straight square duct. *J. Fluid Mech.* **244**, 101–129.
- Gessner, F. B. 1973 The origin of secondary flow in a turbulent flow along a corner. *J. Fluid Mech.* **58** (1), 1–25.
- Gessner, F. B. & Jones, J. B. 1965 On some aspects of fully developed turbulent flow in rectangular channels. *J. Fluid Mech.* **23** (4), 689–713.
- Huser, A. & Biringen, S. 1993 Direct numerical simulation of turbulent flow in a square duct. *J. Fluid Mech.* **257**, 65–95.
- Kim, J. & Moin, P. 1985 Application of a fractional step method to incompressible Navier-Stokes equations. *J. Comput. Phys.* **59**, 308–323.
- Mahesh, K., Constantinescu, G. S. & Moin, P. 2004 A numerical method for large-eddy simulation in complex geometries. *J. Comput. Phys.* **197** (1), 215–240.
- Pinelli, A., Uhlmann, M., Sekimoto, A. & Kuwahara, K. 2010 Reynolds number dependence of mean flow structure in square duct turbulence. *J. Fluid Mech.* **644**, 107–122.
- Schlichting, H. 1979 *Boundary-Layer Theory*. New York: McGraw-Hill.
- Speziale, C. G. 1987 On nonlinear $K-\ell$ and $K-\varepsilon$ models of turbulence. *J. Fluid Mech.* **178** (459–478).
- Uhlmann, M., Pinelli, A., Kawahara, G. & Sekimoto, A. 2007 Marginally turbulent flow in a square duct. *J. Fluid Mech.* **588**, 153–162.
- Wallin, S. & Johansson, A. V. 2000 An explicit algebraic Reynolds stress model for incompressible and compressible turbulent flows. *J. Fluid Mech.* **403**, 89–132.